Flight Dynamics, Control, and Testing of a Coaxial Helicopter UAV with Folding Rotor Blades

Anthony Gong
U.S. Army Combat Capabilities Development Command Aviation & Missile Center
Moffett Field, CA, USA

Mark B. Tischler
Tischler Aeronautics
Sunnyvale, CA, USA

Ohad Shalev-Eggert
Rafael Advanced Defense Systems Ltd.
Haifa, Israel

ABSTRACT

Air launched effects refer to unmanned aerial vehicles deployed from another aircraft. These unmanned aircraft can perform intelligence gathering, surveillance, and reconnaissance in contested areas in place of or prior to the arrival of manned aircraft. A potential air launched effects candidate is the Unmanned Generic Coaxial Rotorcraft which has a cylindrical fuselage, folding rotor blades, and the capability to hover. A series of flight tests were conducted to collect test data for system identification. A bare-airframe flight dynamics model of the vehicle was identified using frequency domain methods and verified in the time domain with doublets. The existing vehicle's PX4 inner-loop flight control system was modeled in Simulink®, combined with the identified hover model, and validated against flight test data. The analysis model was then used to perform multi-objective optimization of the flight control system gains using a comprehensive set of specifications. The optimized control system is shown to have improved tracking and disturbance rejection performance over the baseline in simulation while meeting all desired specifications.

NOTATION

f_a	Nyquist frequency, Hz
f_s	Sampling frequency, Hz
g	Gravity, 9.81 m/s^2
p, q, r	Angular velocities, rad/s
u, v, w	Body-axis velocities, m/s
ϕ	Roll attitude, rad
ψ	Heading, rad
σ	Solidity
θ	Pitch attitude, rad
Ω	Rotor revolution frequency, rad/s
ω_c	Crossover frequency, rad/s

Subscripts

0	Trim state
cmd	Command
cv	Constraint variable
m	Mixer
p	Pilot
s	Sensor location

Acronyms

ALE	Air Launched Effects
DRB	Disturbance Rejection Bandwidth, rad/s
DRP	Disturbance Rejection Peak, dB
GM	Gain Margin, dB
PM	Phase Margin, deg
UGCR	Unmanned Generic Coaxial Rotorcraft

Presented at the Vertical Flight Society's 79th Annual Forum & Technology Display, West Palm Beach, FL, USA, May 16–18, 2023.

INTRODUCTION

Coaxial unmanned aerial vehicle (UAV) configurations (Ref. 1) have the benefit of smaller rotor diameters due to thrust being distributed between the upper and lower rotors. In addition to their compact size, those with rotor blade folding mechanisms (Refs. 2, 3) are suitable for both troop transport and ballistic launch either from the ground or from an aircraft as an air-launched effect (ALE). Such configurations provide a unique combination of portability, hover/low-speed maneuvering capabilities for surveillance and reconnaissance, and a flexible means of deployment to satisfy various mission requirements. The symmetry of the coaxial UAV configurations also simplifies the flight dynamics and control design of the aircraft.

The development of small UAVs has traditionally followed a "fly-fix-fly" approach. The flight control system is typically tuned using an ad-hoc method of trial-and-error and qualitative feedback from the pilot. Model-based approaches leveraging system identification to obtain models of the aircraft initially developed for full-scale aircraft (Ref. 4) have been shown to work well on small-scale UAV (Ref. 5). System identified models used in conjunction with flight control system optimization techniques can further improve performance such as improved disturbance rejection capability (Refs. 6, 7). Stitched models (Ref. 4) of small UAVs (Ref. 8) have recently been developed that expand the analysis and simulation from linear point models to the full flight-envelope and have been

shown to accurately extrapolate for variations in mass properties and airspeed (Ref. 9). These advanced modeling and flight control design techniques can be applied to analyze the flight dynamics and improve the flight control performance for small coaxial helicopter configurations.

In a collaborative effort between the U.S. Army Combat Capabilities Development Command (DEVCOM) Aviation & Missile Center (AvMC) and Rafael Advanced Defense Systems Ltd. that began in 2019 under the U.S./Israel Rotorcraft Project Agreement (RPA), research is being carried out to gain a better understanding of the flight dynamics and control for small coaxial helicopter configurations described above. The Unmanned Generic Coaxial Rotorcraft (UGCR), developed and operated by Rafael, serves as the flight test research vehicle with the objective to expand current knowledge of its flight dynamics and improve upon the performance of the existing flight control system.

This paper starts by describing the flight test vehicle in detail including the hardware modifications to the UGCR and software modifications to PX4 to enable satisfactory flight test data collection. Next, the flight test methodology and associated post-processing of flight data will be described. Then, the identified hover state-space model and the results from system identification are presented. The inner-loop (attitudes and angular rates) flight control system will be covered including the specifications used for optimization and a comparison between baseline and optimized gain sets. Lastly, conclusions based on this joint research effort will be drawn and future work will be discussed.

FLIGHT VEHICLE

The Unmanned Generic Coaxial Rotorcraft (UGCR) was designed and built by Rafael Advanced Defense Systems Ltd. to serve as the research vehicle for the current work (Fig. 1). Its design is aimed to deliver the beneficial ALE-related characteristics of small coaxial UAVs. It is tube-shaped, has a coaxial set of 2-bladed rotors capable of folding parallel to the fuselage, and a tripod-style landing gear for ground stabilization that can also fold parallel to the fuselage. Each of the rotors is driven by a brushless direct-current (BLDC) motor. The vehicle weighs 1.5 kg and has an overall length of 50 cm. Each of the identical rotors has a diameter of 50 cm and a solidity of approximately $\sigma = 0.05$. Additional details on the UGCR can be found in Table 1.

Three servo actuators mounted between the upper and lower rotor systems are used to steer the vehicle in pitch, roll and heave. They simultaneously actuate the control rods connected to both upper and lower swashplates, providing symmetric collective and cyclic pitch changes to both upper and lower rotors. Pitch and roll control are achieved via symmetric deflections of the upper and lower rotor tip path planes, while heave control is achieved through symmetric collective pitch changes on both rotors. A constant difference exists in collective pitch between the upper and lower rotors. It is set by adjusting the lengths of the pushrods, and is calibrated so that the resulting difference in blade drag torque nullifies the yawing moment when both rotors rotate at the same speed in hover since the lower rotor operates in the downwash of the upper rotor. Approximately 2 degrees of additional collective pitch in the lower rotor was found to be the appropriate difference for the nominal working rotor rotational speed of 4000 RPM. Yaw control is achieved via differential RPM of the two motors.

Figure 1: Unmanned Generic Coaxial Rotorcraft (UGCR) by Rafael Ltd.

The onboard flight control computer (FCC) is a Pixhawk 4 running the PX4 autopilot firmware, which was modified to include several additional features: RPM feedback and control; increased sample rate of up to 1 kHz required for anti-aliasing post-processing; and sweep generator that provides the capability to inject automated frequency sweeps to excite the vehicle for system identification. The automated sweep generator enables the user to select the swept frequency range, the control axis, and location where the signal is injected (i.e. rate or attitude). The sweep generator and its interaction with a simplified schematic of the inner-loop flight control system is depicted in Fig. 2.

FLIGHT TESTS

Flight tests were planned and executed to supply the necessary data for frequency domain system identification using the CIFER® software (Ref. 4). The core of the required data were frequency sweeps for identification and doublets for verification. Frequency sweeps are continuous sinusoidal inputs of increasing frequency designed to excite a vehicle's dynamics over a desired frequency range. The commanded inputs and resulting vehicle states are used to identify frequency responses for system identification. Doublets are composed of two, short, step inputs in opposing directions, primarily used as a dissimilar signal for time domain validation of the to-be-identified model.

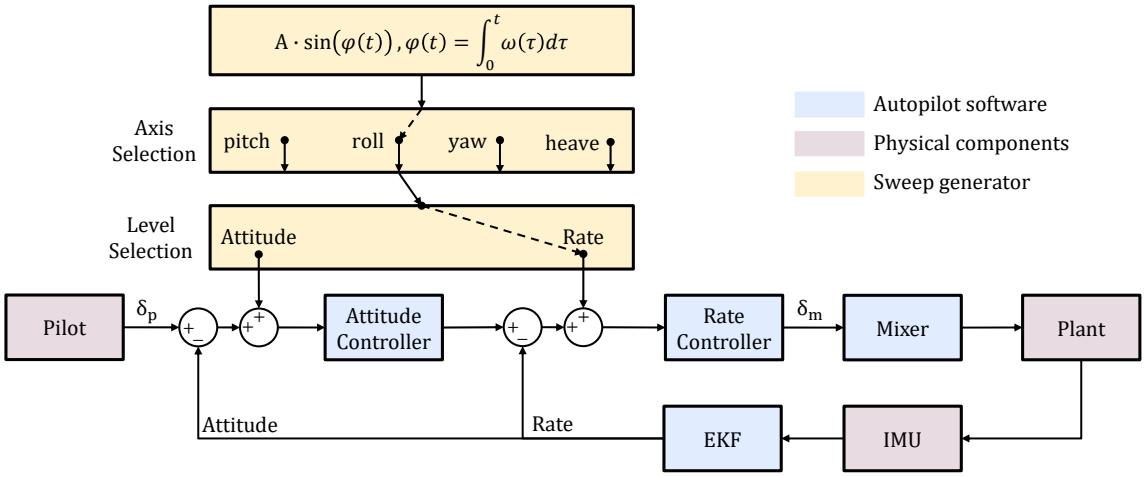

Figure 2: Schematic of sweep generator integration with autopilot software.

Table 1: UGCR properties.

Rotors	
Number of Rotors	2
Diameter [cm]	50
Blades Per Rotor	2
Blades Model	Alight 205
Root Chord [cm]	2.5
Tip Chord [cm]	1.9
Fuselage	
Shape	Cylinder
Diameter [cm]	8
Length [cm]	30
Overall	
Length [cm]	50
Mass [kg]	1.5

The vehicle is trimmed at the nominal flight condition (hover, in this case) for several seconds prior to initiating and after completing either sweep or doublet test signals. Figure 3a provides an example of the test approach that includes first putting the vehicle in a hover trim state, performing a frequency sweep for a given axis (e.g. pitch), letting the vehicle return to trim, executing a doublet maneuver in the same axis, and then finishing up by returning the vehicle to hover trim for several seconds. This progression of events can also be seen in Fig. 3b where the pilot manually sweeps the pitch axis through the transmitter input (δ_{lon_p}), the pitch axis control system commands an input to the mixer (δ_{lon_m}), and the vehicle's pitch attitude (θ) responds accordingly.

Frequency sweeps and doublets around hover were collected in all four axes. Sweeps were flown both manually, prior to the completion of the automated sweep generator, and automatically, thereafter. Each maneuver was flown multiple times per axis. This multitude of frequency sweeps increases the frequency content of the database and reduces the sus-

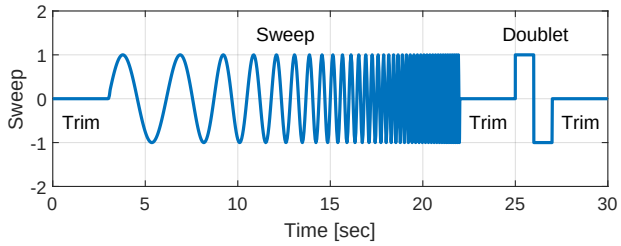

(a) Sample progression of trim, sweep, and doublet inputs.

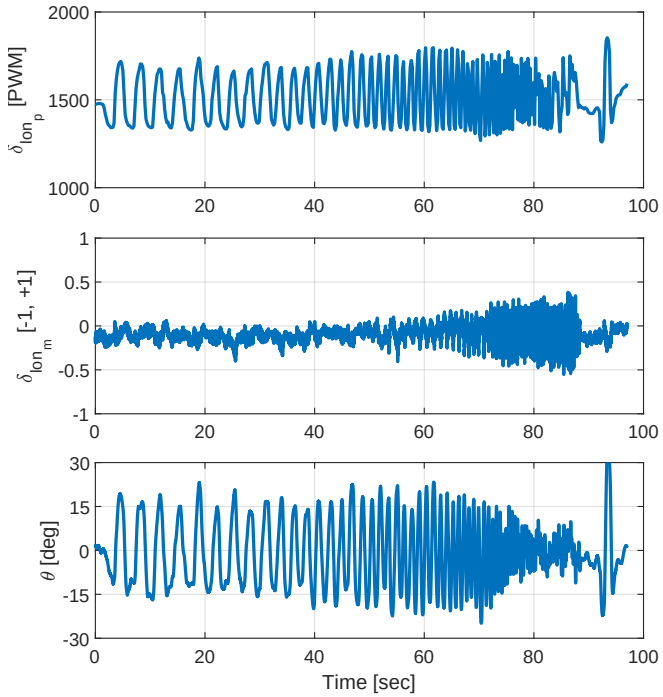

(b) Time history of a pitch axis frequency sweep and doublet.

Figure 3: Time history progression of test points.

ceptibility to random noise and turbulence effects through additional averaging and assists in identifying a more accurate model (Ref. 4). Table 2 summarizes the number of frequency sweeps collected at the hover flight condition over the course of this work. It should be noted that the large number of sweeps is not needed for identification (typically only 2-3 sweeps per axis is sufficient), but rather a consequence of addressing hardware, software, and data quality issues over the course of the ongoing research. Due to the differing nature of the aircraft's hardware configuration during the course of data collection, a smaller subset of the sweeps and doublets were used for identification and verification.

Table 2: Number of hover frequency sweeps and doublets collected over the course of the current work.

	Roll	Pitch	Yaw	Heave
Manual Sweep	14	12	7	6
Automated Sweep	2	4	2	0
Doublet	7	13	11	6

Flights around the hover flight condition were conducted in an outdoor enclosure for safety and regulatory reasons. Extra attention had to be given to the beginning portion of the frequency sweep while exciting the vehicle response since the longer time periods at low-frequency results in larger position displacements and could lead to impact with the enclosing net.

Data Reduction and Processing

The data collected from flight tests were post-processed through a series of steps including format conversion, anti-alias filtering, re-sampling, and analysis to select desired segments within the flight logs with frequency sweep and doublet time histories.

High-frequency vehicle vibrations were problematic for data analysis. Specifically, the accelerometers signals contained measurements in excess of ± 15 m/s^2 during initial flight tests when the magnitude is expected to be on the order of ± 1 m/s^2. Attempts to physically dampen vibrations including mounting the FCC on a vibration isolation platform, using vibration dampening foam, and using a different FCC that contains vibration-damped IMU boards did not alleviate the problem.

Figure 4 shows the power spectral density (PSD) of the x-axis accelerometer from flight test data logged at both 250 Hz and 1 kHz. The 2-bladed rotors of the UGCR spin at a nominal speed of 4000 RPM. Peaks in the PSD corresponding to the 1/rev ($\Omega = 419$ rad/s $= 66.7$ Hz) and 2/rev ($2\Omega = 838$ rad/s $= 133.3$ Hz) frequencies can be clearly seen in the signal sampled at 1 kHz. The PX4 sample rate of 250 Hz initially used for data collection was insufficient to capture high frequency spectral content and resulted in an aliased signal due to the folding of higher frequency harmonics about the Nyquist frequency of $f_A = 125$ Hz. The folding of the 2/rev frequency about the Nyquist frequency results in a dominant peak in the aliased signal at a frequency of $f' = 116.7$ Hz (i.e. $f' = 2f_A - 2\Omega$). The 1/rev frequency is properly captured since it is below the Nyquist frequency of both sample rates. However, the magnitude is significantly higher for the $f_s = 250$ Hz signal due to the effect of aliasing.

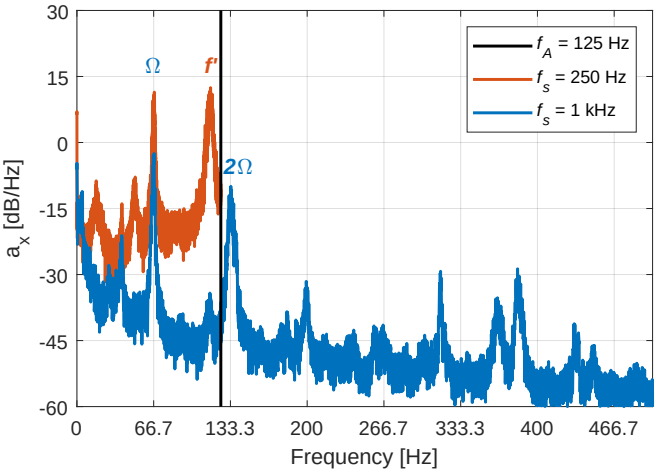

Figure 4: Power spectral density of the x-axis accelerometer signal sampled at 250 Hz and 1 kHz showing peaks at integer multiples of rotor frequency.

The PX4 autopilot firmware was modified to enable sampling at 1 kHz (15 times faster than the 1/rev frequency of 66.7 Hz). Hardware modifications included replacing the Pixhawk 2 FCC with a Pixhawk 4 for its faster CPU and replacing the microSD card with one capable of faster write speeds to support logging at the higher sample rate. Figure 5 shows the x-axis accelerometer signal simultaneously sampled at 250 Hz and 1 kHz during a pitch axis frequency sweep. The signal sampled at 250 Hz contains measurements in excess of ± 15 m/s^2 (an effect of aliasing due to undersampling) while the same sensor sampled at 1 kHz has significantly reduced magnitude, on the order of ± 3 m/s^2.

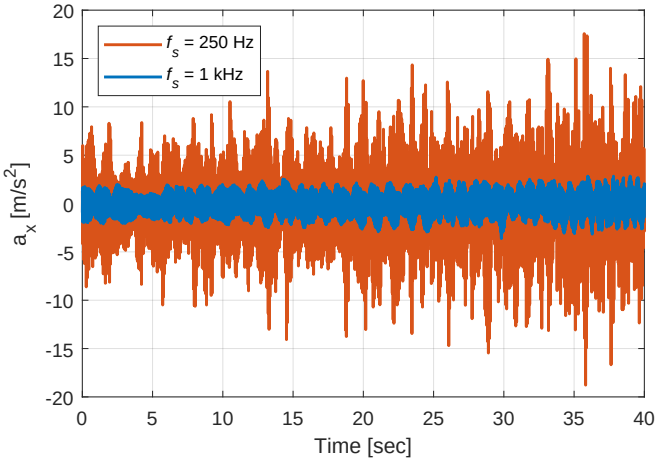

Figure 5: X-axis accelerometer data simultaneously sampled at 250 Hz and 1 kHz during a pitch axis frequency sweep.

A 4$^{\text{th}}$-order Butterworth filter with a cutoff frequency of 30 Hz was designed and applied both forwards and backwards to

the flight data to prevent additional phase lag from the filter. Figure 6 presents the unfiltered x-axis accelerometer signal sampled at 1 kHz during a pitch axis frequency sweep along with the post-processed signal. The post-processed signal is seen to recover the expected sinusoidal shape matching the progression of the frequency sweep that was used to excite the vehicle and have lower magnitude (± 1 m/s^2) due to the low-pass filter attenuating high frequency noise above 30 Hz.

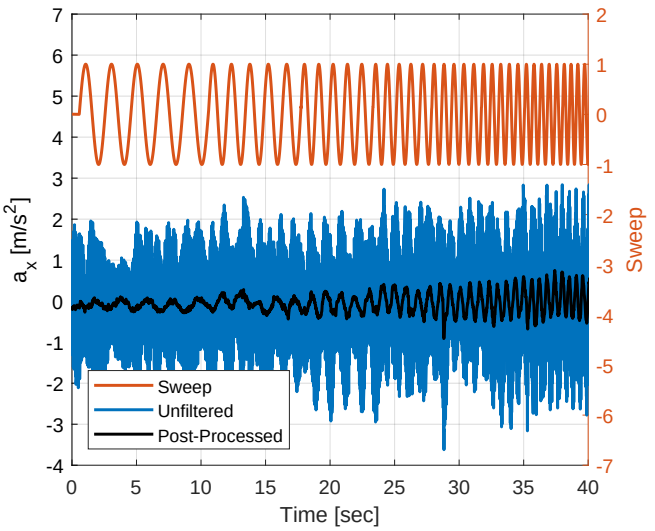

Figure 6: X-axis accelerometer signal sampled at 1 kHz during a pitch axis frequency sweep prior to and after post processing.

HOVER STATE-SPACE MODEL IDENTIFICATION

The CIFER® software package (Ref. 4) was used to generate frequency responses from the frequency sweeps collected during flight tests, identify a state-space model (Eq. 1) of the bare-airframe dynamics at the hover flight condition, and verify the model accuracy in the time domain using doublets.

$$\begin{aligned} \mathbf{M}\dot{\mathbf{x}} &= \mathbf{F}\mathbf{x} + \mathbf{G}\mathbf{u}(t-\boldsymbol{\tau}) \\ \mathbf{y} &= \mathbf{H_0}\mathbf{x} + \mathbf{H_1}\dot{\mathbf{x}} \end{aligned} \tag{1}$$

Hover Model Structure

A six degree-of-freedom (6-DOF) model structure was used for identification. Additionally, extra states, inputs, and outputs were included to implement constraint equations and sensor offsets. Equations 2-7 provide the expanded forms of the matrices from Eq. 1 and are used as a starting point for the identification.

$$\mathbf{M} = \begin{bmatrix} I_{6\times6} & 0_{6\times5} & 0_{6\times3} \\ 0_{5\times6} & I_{5\times5} & 0_{5\times3} \\ Z_{3\times6} & 0_{3\times5} & I_{3\times3} \end{bmatrix}$$
$$\mathbf{Z} = \begin{bmatrix} -1 & 0 & 0 & 0 & -z_a & y_a \\ 0 & -1 & 0 & z_a & 0 & -x_a \\ 0 & 0 & -1 & -y_a & x_a & 0 \end{bmatrix} \tag{2}$$

$$\mathbf{G} = \begin{bmatrix} X_{\text{lat}} & X_{\text{lon}} & X_{\text{col}} & X_{\text{yaw}} & 0 & 0 \\ Y_{\text{lat}} & Y_{\text{lon}} & Y_{\text{col}} & Y_{\text{yaw}} & 0 & 0 \\ Z_{\text{lat}} & Z_{\text{lon}} & Z_{\text{col}} & Z_{\text{yaw}} & 0 & 0 \\ L_{\text{lat}} & L_{\text{lon}} & L_{\text{col}} & L_{\text{yaw}} & 0 & 0 \\ M_{\text{lat}} & M_{\text{lon}} & M_{\text{col}} & M_{\text{yaw}} & 0 & 0 \\ N_{\text{lat}} & N_{\text{lon}} & N_{\text{col}} & N_{\text{yaw}} & 0 & 0 \\ 0_{3\times1} & 0_{3\times1} & 0_{3\times1} & 0_{3\times1} & 0_{3\times1} & 0_{3\times1} \\ 0 & 0 & 0 & 0 & 0 & -g \\ 0 & 0 & 0 & 0 & g & 0 \\ 0_{3\times1} & 0_{3\times1} & 0_{3\times1} & 0_{3\times1} & 0_{3\times1} & 0_{3\times1} \end{bmatrix} \tag{4}$$

$$\mathbf{H_0} = \begin{bmatrix} 0_{3\times3} & 0_{3\times3} & 0_{3\times3} & 0_{3\times2} & 0_{3\times3} \\ 0_{3\times3} & I_{3\times3} & 0_{3\times3} & 0_{3\times2} & 0_{3\times3} \\ 0_{3\times3} & 0_{3\times3} & J_{3\times3} & 0_{3\times2} & 0_{3\times3} \\ 0_{2\times3} & 0_{2\times3} & 0_{2\times3} & I_{2\times2} & 0_{2\times3} \end{bmatrix} \tag{5}$$
$$\mathbf{J} = \begin{bmatrix} 0 & g & 0 \\ -g & 0 & 0 \\ 0 & 0 & 0 \end{bmatrix}$$

$$\mathbf{H_1} = \begin{bmatrix} 0_{3\times11} & I_{3\times3} \\ 0_{3\times11} & 0_{3\times3} \\ 0_{3\times11} & I_{3\times3} \\ 0_{2\times11} & 0_{2\times3} \end{bmatrix} \tag{6}$$

$$\boldsymbol{\tau} = \begin{bmatrix} \tau_{\text{lat}} & \tau_{\text{lon}} & \tau_{\text{col}} & \tau_{\text{yaw}} & 0 & 0 \end{bmatrix}^{\text{T}} \tag{7}$$

The state vector $\mathbf{x}$ (Eq. 8) is comprised of the body-axis velocities at the center of gravity (CG) (u, v, w), angular velocities (p, q, r), Euler angles (ϕ, θ, ψ), forward and lateral body-axis velocities at the CG used as constraint variables (u_{cv}, v_{cv}), and body-axis velocities at the sensor location (u_s, v_s, w_s).

$$\mathbf{x} = \begin{bmatrix} u & v & w & p & q & r & \phi & \theta & \psi & u_{cv} & v_{cv} & u_s & v_s & w_s \end{bmatrix}^{\text{T}} \tag{8}$$

The input vector $\mathbf{u}$ (Eq. 9) consists of the mixer input channels for the four axes ($\delta_{\text{lat}_\text{m}}$, $\delta_{\text{lon}_\text{m}}$, $\delta_{\text{col}_\text{m}}$, $\delta_{\text{yaw}_\text{m}}$) and two Euler angles used as constraint variables (ϕ_{cv}, θ_{cv}).

$$\mathbf{u} = \begin{bmatrix} \delta_{\text{lat}_\text{m}} & \delta_{\text{lon}_\text{m}} & \delta_{\text{col}_\text{m}} & \delta_{\text{yaw}_\text{m}} & \phi_{cv} & \theta_{cv} \end{bmatrix}^{\text{T}} \tag{9}$$

The output vector $\mathbf{y}$ (Eq. 10) consists of the body-axis accelerations at the sensor locations ($\dot{u}_s$, $\dot{v}_s$, $\dot{w}_s$) reconstructed from inertial measurements as shown in Eq. 11 (Ref. 4), angular velocities (p, q, r), accelerometer measurements at the sensor locations (a_{x_s}, a_{y_s}, a_{z_s}), and two body-axis velocities at the CG (u_{cv}, v_{cv}).

$$\mathbf{y} = \begin{bmatrix} \dot{u}_s & \dot{v}_s & \dot{w}_s & p & q & r & a_{x_s} & a_{y_s} & a_{z_s} & u_{cv} & v_{cv} \end{bmatrix} \tag{10}$$

$$\begin{aligned} \dot{u}_s &= a_{x_s} - W_0 q + V_0 r - (g\,\cos\Theta_0)\theta \\ \dot{v}_s &= a_{y_s} - U_0 r + W_0 p + (g\,\cos\Theta_0)\phi \\ \dot{w}_s &= a_{z_s} - V_0 p + U_0 q - (g\,\sin\Theta_0)\theta \end{aligned} \tag{11}$$

$$\mathbf{F} = \begin{bmatrix}
X_u & X_v & X_w & X_p & X_q - W_0 & X_r + V_0 & 0 & -g\cos(\Theta_0) & 0 & 0 & 0 & 0_{1\times3} \\
Y_u & Y_v & Y_w & Y_p + W_0 & Y_q & Y_r - U_0 & g\cos(\Theta_0) & 0 & 0 & 0 & 0 & 0_{1\times3} \\
Z_u & Z_v & Z_w & Z_p - V_0 & Z_q + U_0 & Z_r & 0 & -g\sin(\Theta_0) & 0 & 0 & 0 & 0_{1\times3} \\
L_u & L_v & L_w & L_p & L_q & L_r & 0 & 0 & 0 & 0 & 0 & 0_{1\times3} \\
M_u & M_v & M_w & M_p & M_q & M_r & 0 & 0 & 0 & 0 & 0 & 0_{1\times3} \\
N_u & N_v & N_w & N_p & N_q & N_r & 0 & 0 & 0 & 0 & 0 & 0_{1\times3} \\
0 & 0 & 0 & 1 & 0 & \tan(\Theta_0) & 0 & 0 & 0 & 0 & 0 & 0_{1\times3} \\
0 & 0 & 0 & 0 & 1 & 0 & 0 & 0 & 0 & 0 & 0 & 0_{1\times3} \\
0 & 0 & 0 & 0 & 0 & \sec(\Theta_0) & 0 & 0 & 0 & 0 & 0 & 0_{1\times3} \\
0 & 0 & 0 & 0 & 0 & 0 & 0 & 0 & 0 & X_{u_{cv}} & 0 & 0_{1\times3} \\
0 & 0 & 0 & 0 & 0 & 0 & 0 & 0 & 0 & 0 & Y_{v_{cv}} & 0_{1\times3} \\
0_{3\times1} & 0_{3\times1} & 0_{3\times1} & 0_{3\times1} & 0_{3\times1} & 0_{3\times1} & 0_{3\times1} & 0_{3\times1} & 0_{3\times1} & 0_{3\times1} & 0_{3\times1} & 0_{3\times3}
\end{bmatrix} \tag{3}$$

The aircraft CG is located *above* the sensors contained within the Pixhawk 4 FCC. The aircraft CG and sensor location were measured to be 17 and 45 mm from the top of the fuselage, respectively, giving a vertical sensor offset of $z_a = 28$ mm. The offsets in the x and y directions were negligible due to aircraft symmetry ($x_a = y_a = 0$). The known sensor offsets (x_a, y_a, z_a) in Eq. 12 are incorporated into Eq. 2 to correct the model to the sensors during the system identification process. This approach of including the sensor offset terms in the mass matrix through the use of constraint equations provides the flexibility of setting the sensor offset terms as identification parameters. Since the sensor offset terms could be reliably measured in this case, they were fixed during the identification process.

$$\begin{aligned}
a_{x_s} &= \dot{u} + W_0 q - V_0 r + (g\ \cos\Theta_0)\theta + z_a\dot{q} - y_a\dot{r} \\
a_{y_s} &= \dot{v} + U_0 r - W_0 p - (g\ \cos\Theta_0)\phi - z_a\dot{p} + x_a\dot{r} \\
a_{z_s} &= \dot{w} + V_0 p - U_0 q + (g\ \sin\Theta_0)\theta + y_a\dot{p} - x_a\dot{q}
\end{aligned} \tag{12}$$

The speed-damping derivatives (X_u, Y_v) could not be accurately identified due to a lack of low-frequency coherence in the on-axis frequency responses (e.g. $\dot{u}/\delta_{\text{lon}_\text{m}}$, $q/\delta_{\text{lon}_\text{m}}$, $a_x/\delta_{\text{lon}_\text{m}}$). Equations 13-14 were used as a low-frequency approximation of the longitudinal and lateral force responses (Ref. 4) and embedded in the state-space formulation to isolate the speed-damping derivatives and constrain them to their respective counterparts (i.e. $X_u = X_{u_{cv}}$, $Y_v = Y_{v_{cv}}$).

$$\dot{u}_{cv} = X_{u_{cv}} u_{cv} - g\theta_{cv} \tag{13}$$

$$\dot{v}_{cv} = Y_{v_{cv}} v_{cv} + g\phi_{cv} \tag{14}$$

The advantage of using Eqs. 13-14 can be seen in the transfer function equivalents in Eqs. 15-16 that use measured aircraft outputs (ϕ, θ, $\dot{u}$, $\dot{v}$) to form the frequency responses. These kinematically consistent aircraft outputs have good energy content at lower frequencies due to excitation from sources besides the control mixer inputs (e.g. wind, turbulence). As a result, these responses generally have better coherence at lower frequencies than the on-axis frequency responses for control inputs. An example of this can be seen in Fig. 7 where the on-axis responses ($\dot{u}/\delta_{\text{lon}_\text{m}}$, $\dot{q}/\delta_{\text{lon}_\text{m}}$) have good coherence down to 0.50 rad/s, whereas the u_{cv}/θ_{cv} response used for isolating the X_u has excellent coherence at frequencies as low as 0.15 rad/s.

$$\frac{\dot{u}_{cv}}{\theta_{cv}}(s) = \frac{-sg}{s - X_{u_{cv}}} \tag{15}$$

$$\frac{\dot{v}_{cv}}{\phi_{cv}}(s) = \frac{sg}{s - Y_{v_{cv}}} \tag{16}$$

Identification Results

Figure 7 shows the identification results for the longitudinal axis. The identified model is shown to overlay well against the flight test data across a wide range of frequencies for the on-axis responses as well as the u_{cv}/θ_{cv} response used to identify the X_u derivative from Eq. 13.

The identified parameters of the 6-DOF model are shown in Table 3. In general, the identified parameters meet the guidelines for Cramér-Rao bound percentages (CR%$\leq$20%) and insensitivities (I%$\leq$10%). The speed-damping derivatives are above these thresholds and were identified to be slightly positive values rather than negative as would have been expected. The use of the responses from Eqs. 15-16 enabled good coherence to lower frequencies than those from the mixer inputs, but the effect of the speed damping derivatives exist at even lower frequencies than those available in the flight data to accurately identify for this vehicle.

The heave rate damping derivative, Z_w, was found to be insensitive during the accuracy analysis portion of the system identification and therefore fixed to zero. While the Z_w term physically exists, it has negligible influence on the flight dynamics at frequencies of interest. Similar to the speed-damping derivatives, the effect of Z_w primarily exists at low frequency, but the on-axis $a_z/\delta_{\text{col}_\text{m}}$ response only had good coherence down to 0.80 rad/s.

Minor differences in the roll and pitch axes were expected due to the placement of internal components (FCC, battery), so the roll and pitch axes parameters were not constrained to one another during identification. Nonetheless, there is strong symmetry in the identified stability and control derivatives in the roll and pitch axes as expected for this coaxial UAV configuration (e.g. $L_p \approx M_q$, $L_{\delta_{\text{lat}}} \approx M_{\delta_{\text{lon}}}$).

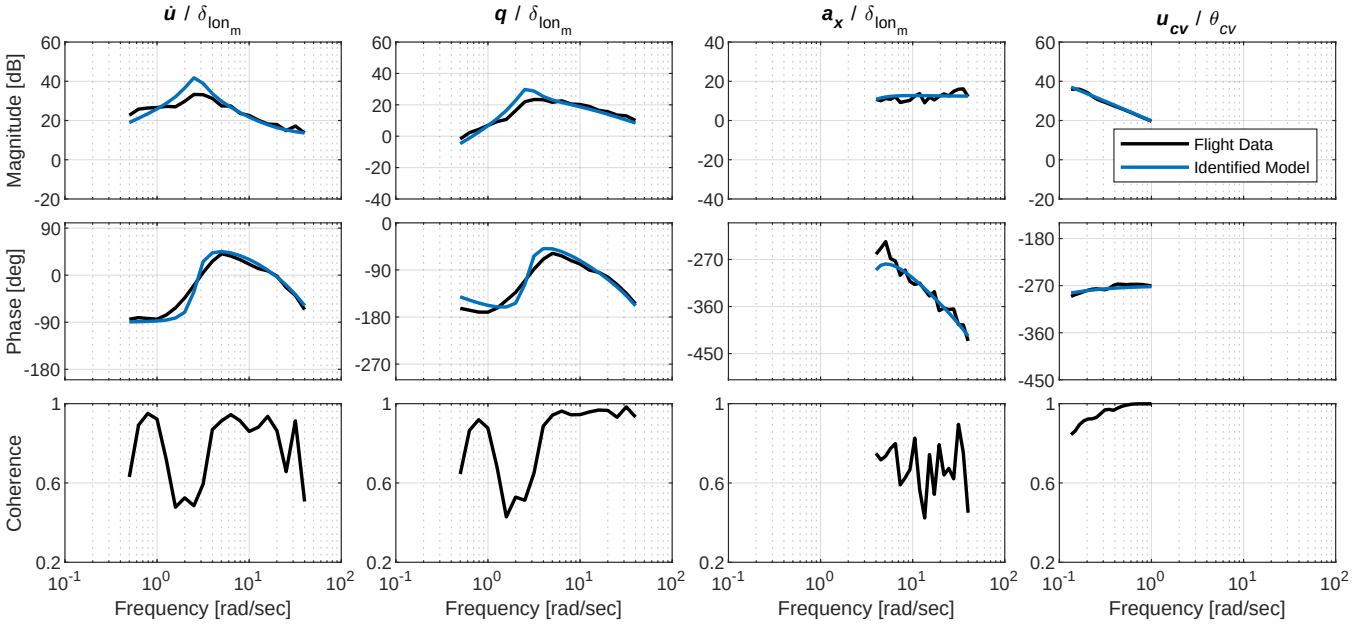

Figure 7: Identification of UGCR at hover flight condition.

Table 4 shows the frequency domain mismatch cost functions, J, for each frequency response used in the identification as well as the average cost function J_{ave}. The average frequency domain mismatch cost function of J_{ave} =78.2 indicates that the current identified hover model is good. An average cost function less than J_{ave} =100 is considered acceptable and less than J_{ave} =50 is considered a perfect model.

The eigenvalues of the hover model can be seen in Fig. 8. The lateral and longitudinal axes each have 3 eigenvalues making up the characteristic "hovering cubic" with a stable real pole in the left half plane and an unstable pair on the right half plane. The heave and yaw axes eigenvalues are real poles located at their respectively identified stability derivative (i.e., yaw axis eigenvalue at N_r = -6.92, heave axis eigenvalue at Z_w = 0). The unstable bare-airframe dynamics at hover necessitates a properly designed and tuned flight control system for stable flight.

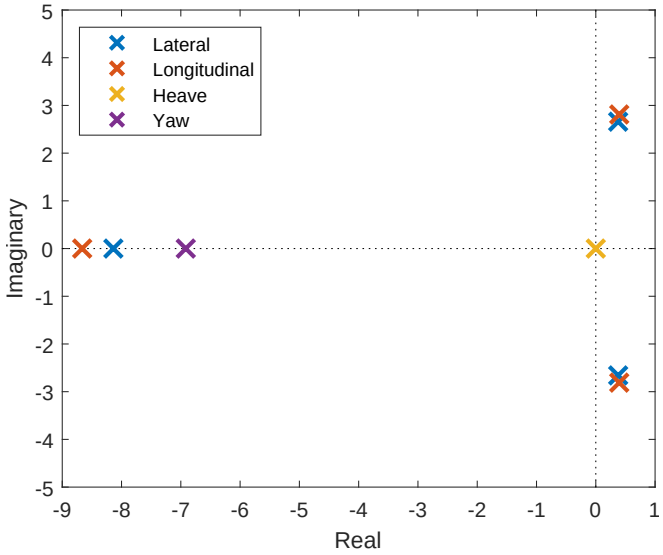

Figure 8: Hover model eigenvalues.

Time Domain Verification

The identified hover model was verified in the time domain through the use of doublet flight test data. The mixer channel inputs from all four axes are used as inputs to the bare-airframe model and the resulting outputs are compared against flight data. Figure 9 shows that the model response closely tracks the key roll axis outputs during a large roll doublet maneuver that exceeds 150 deg/s. Similar results were seen in other axes.

FLIGHT CONTROL SYSTEM OPTIMIZATION

PX4 Inner-Loop Flight Control System

The inner-loops of the PX4 flight control system, shown in Fig. 10, use a cascaded architecture controlling the angular rates and attitudes of the aircraft. Specifically, the attitude loops use a simple proportional gain while the angular rate loops use a PID architecture with a feed-forward element. F_ω and $F_{\dot{\omega}}$ are low-pass filters with 30 Hz and 80 Hz cutoff frequencies, respectively. These low-pass filter parameters were not tuned during the optimization process.

Table 3: Identified parameters of the UGCR.

Parameter	Value	CR%	I%
X_u	0.05[a]	23.24	11.34
Y_v	0.03[a]	34.03	16.58
Z_w	0[b]	—	—
X_q	0.15	34.69	6.46
Y_p	-0.18	28.91	5.33
L_v	-7.33	6.79	1.90
M_u	6.24	6.61	1.75
L_p	-8.22	7.16	1.31
M_q	-7.88	7.01	1.34
N_r	-6.92	10.02	3.32
$X_{\delta_{\text{lon}}}$	-6.34	12.25	1.49
$Y_{\delta_{\text{lat}}}$	5.73	12.76	1.48
$Z_{\delta_{\text{col}}}$	-44.33	3.80	1.90
$L_{\delta_{\text{lat}}}$	106.1	4.83	0.79
$M_{\delta_{\text{lon}}}$	107.4	4.77	0.84
$N_{\delta_{\text{yaw}}}$	936.7	5.76	2.03
τ_{lat}	0.032	6.36	2.48
τ_{lon}	0.035	6.39	2.53
τ_{col}	0.033	7.73	3.87
τ_{yaw}	0.012	25.84	11.51

[a] Constrained parameter.
[b] Fixed parameter.

Analysis Model

The PX4 inner-loop architecture was replicated in Simulink® for analysis, simulation, and optimization from available documentation and the open-source code base. The Simulink® representation of the flight control system was combined with the identified hover model and and the entire closed-loop system validated against flight test data. The constraint variable inputs, states, and outputs of the hover model are not included in the bare-airframe of the analysis model as they do not affect the flight dynamics of the vehicle.

Figure 11 shows a comparison of the flight test responses against the simulated responses by injecting a piloted doublet input $[\delta_{\text{lat}_p} \quad \delta_{\text{lon}_p} \quad \delta_{\text{col}_p} \quad \delta_{\text{yaw}_p}]^{\text{T}}$ from flight test data into the closed-loop simulation. The PX4 parameters defining the baseline flight control gains and control system limits were loaded into the analysis model to replicate the flight test conditions in simulation. An excellent match is seen between the flight test data and simulation simultaneously indicating that the bare-airframe model was accurately identified

Table 4: Individual and average cost for the hover model.

Response	Cost
$\dot{v}/\delta_{\text{lat}_m}$	125.2
p/δ_{lat_m}	134.6
$a_y/\delta_{\text{lat}_m}$	65.3
$\dot{u}/\delta_{\text{lon}_m}$	153.2
q/δ_{lon_m}	155.3
$a_x/\delta_{\text{lon}_m}$	108.4
$a_z/\delta_{\text{col}_m}$	14.9
r/δ_{yaw_m}	12.0
u_{cv}/θ_{cv}	3.1
v_{cv}/ϕ_{cv}	10.2
$\mathbf{J}_{\text{ave}}$	**78.2**

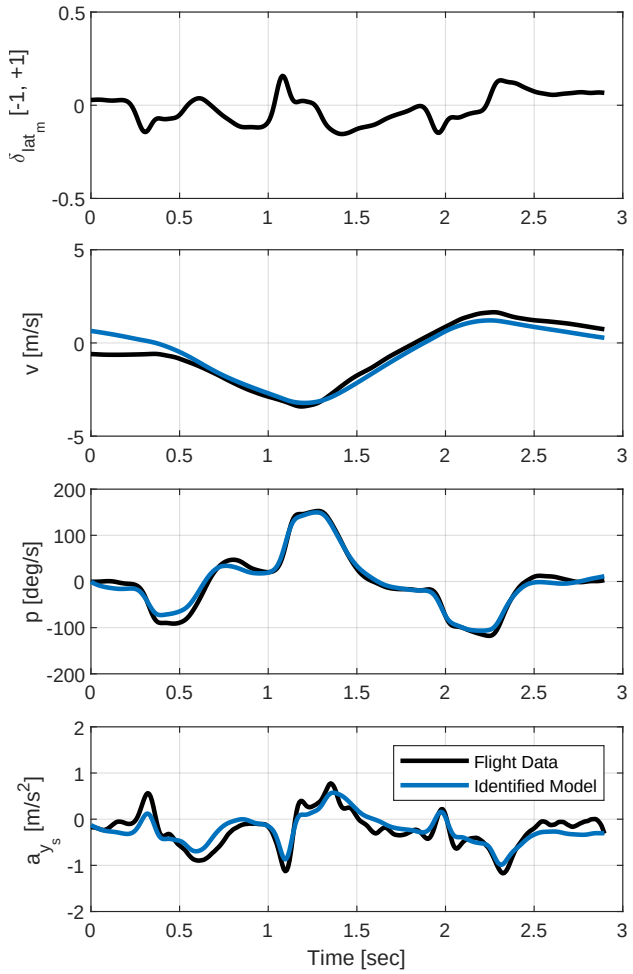

Figure 9: Time domain verification of the identified bare-airframe model using a roll doublet.

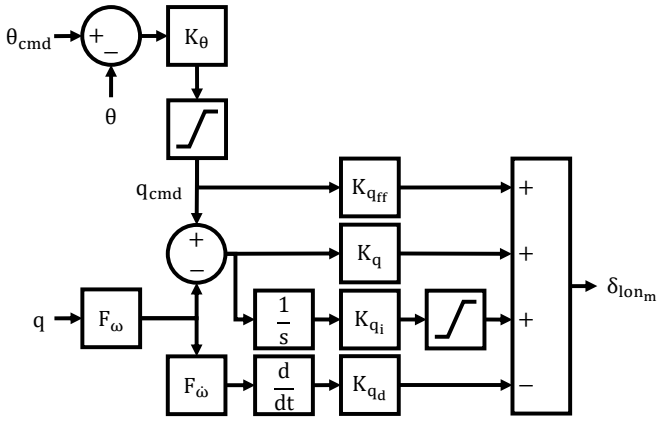

Figure 10: PX4 pitch axis inner-loop block diagram.

and that the crucial flight control system elements were properly replicated in simulation. An example of this can be seen in Fig. 11 at the 3-second mark where the PX4 parameter *MC_PITCHRATE_MAX* limits the pitch rate command (q_{cmd}) from the attitude control system to a maximum of $\pm$100 deg/s during the doublet maneuver.

Optimization Approach

The flight control system gains were selected as design parameters and optimized using CONDUIT® (Ref. 10) against a comprehensive set of specifications (Table 5) ensuring desired stability and performance with minimal actuator effort. This optimization approach allows the designer to group specifications into three distinct categories: hard constraints, soft constraints, and summed objectives. The optimization process attempts to first meet all hard constraints during Phase 1 of the optimization. Then, it optimizes the design parameters to meet specifications designated as soft constraints in Phase 2 while maintaining all hard constraints. Lastly, the summed objectives are minimized in Phase 3.

Table 5: CONDUIT® optimization specifications.

Spec Name	Description	Axes[a]
	Hard Constraints	
EigLcG1	Closed-loop eigenvalues	All
NicMgG2	Nichols margin	All
StbMgG2	Gain and phase margins	All
	Soft Constraints	
CrsMnG2	Minimum crossover frequency	All
DstBwG1	Disturbance rejection bandwidth	All
DstPkG1	Disturbance rejection peak	All
EigDpG2	Closed-loop damping ratio	All
FrqDpG2	Frequency response magnitude	R, P
	Summed Objectives	
CrsLnG1	Maximum crossover frequency	All
RmsAcG1	Actuator RMS	All

[a] R = Roll, P = Pitch, H = Heave, Y = Yaw

Stability-oriented specifications (EigLcG1, NicMgG2, StbMgG2) are set as hard constraints to prioritize and maintain closed-loop stability throughout the three phases of optimization. These specifications ensure that the closed-loop poles are in the left-half-plane (LHP) and that each axes' broken-loop response meets the Nichols margin and stability margin requirements. In this case, both NicMgG2 and StbMgG2 specifications use boundaries with 10% increased margins (e.g. GM$\geq$6.6 dB and PM$\geq$50 degrees) in anticipation of nested outer position and velocity loops that will degrade the inner-loop stability margins (Ref. 10).

The soft constraints included minimum crossover frequency (CrsMnG2), disturbance rejection bandwidth (DRB, DstBwG1) and peak (DRP, DstPkG1) specifications (Ref. 11) to increase robustness and disturbance rejection performance. The EigDpG2 specification was used to ensure that the closed-loop damping ratio is above a desired threshold. The FrqDpG2 specification was also included to improve the attitude tracking performance in the pitch and roll axes by ensuring that the closed-loop magnitude responses at low-frequency were within a desired tolerance of the expected steady-state gain.

Once all other design requirements are met, two specifications are minimized as summed objectives in Phase 3 of the optimization. The CrsLnG1 specification is used to reduce the crossover frequency in each axis (without violating CrsMnG2) to prevent over-driving of the actuators. The RmsAcG1 specification computes the actuator position root-mean-square (RMS) to pilot input and is used to minimize the actuator activity. This minimization these summed objectives in this phase of the optimization ensures that the solution meets the design specifications with minimum control effort (Ref. 10).

Optimization Results

A total of 14 design parameters were optimized and a comparison of the baseline and optimized values and results can be seen in Tables 6-7. The roll, pitch, and yaw axes feed-forward gains ($K_{p_{ff}}$, $K_{q_{ff}}$, $K_{r_{ff}}$) were fixed to zero since they were found to be correlated with their respective attitude gains due to being connected in series (Fig. 10) and therefore have a redundant effect as design parameters.

Table 6: Baseline versus optimized design parameters.

Axis	Parameter	Baseline	Optimized	% Change
Roll	K_ϕ	6.0000	8.4319	41
	$K_{p_{ff}}$	0.0500	0.0000[a]	-100
	K_p	0.1200	0.1847	54
	K_{p_i}	0.0100	1.5187	15087
	K_{p_d}	0.0012	0.0039	223
Pitch	K_θ	6.0000	7.9794	33
	$K_{q_{ff}}$	0.0500	0.0000[a]	-100
	K_q	0.1200	0.1941	62
	K_{q_i}	0.0100	1.3341	13241
	K_{q_d}	0.0012	0.0036	201
Yaw	K_ψ	5.0000	5.5841	12
	K_{rff}	0.0030	0.0000[a]	-100
	K_r	0.0600	0.0320	-47
	K_{r_i}	0.0120	0.0256	113
	K_{r_d}	0.0000	0.0000[a]	—
Heave	K_h	0.2000	0.1481	-26
	K_{h_i}	0.0200	0.0107	-46
	K_{h_d}	0.0000	0.0124	—

[a] Fixed parameter

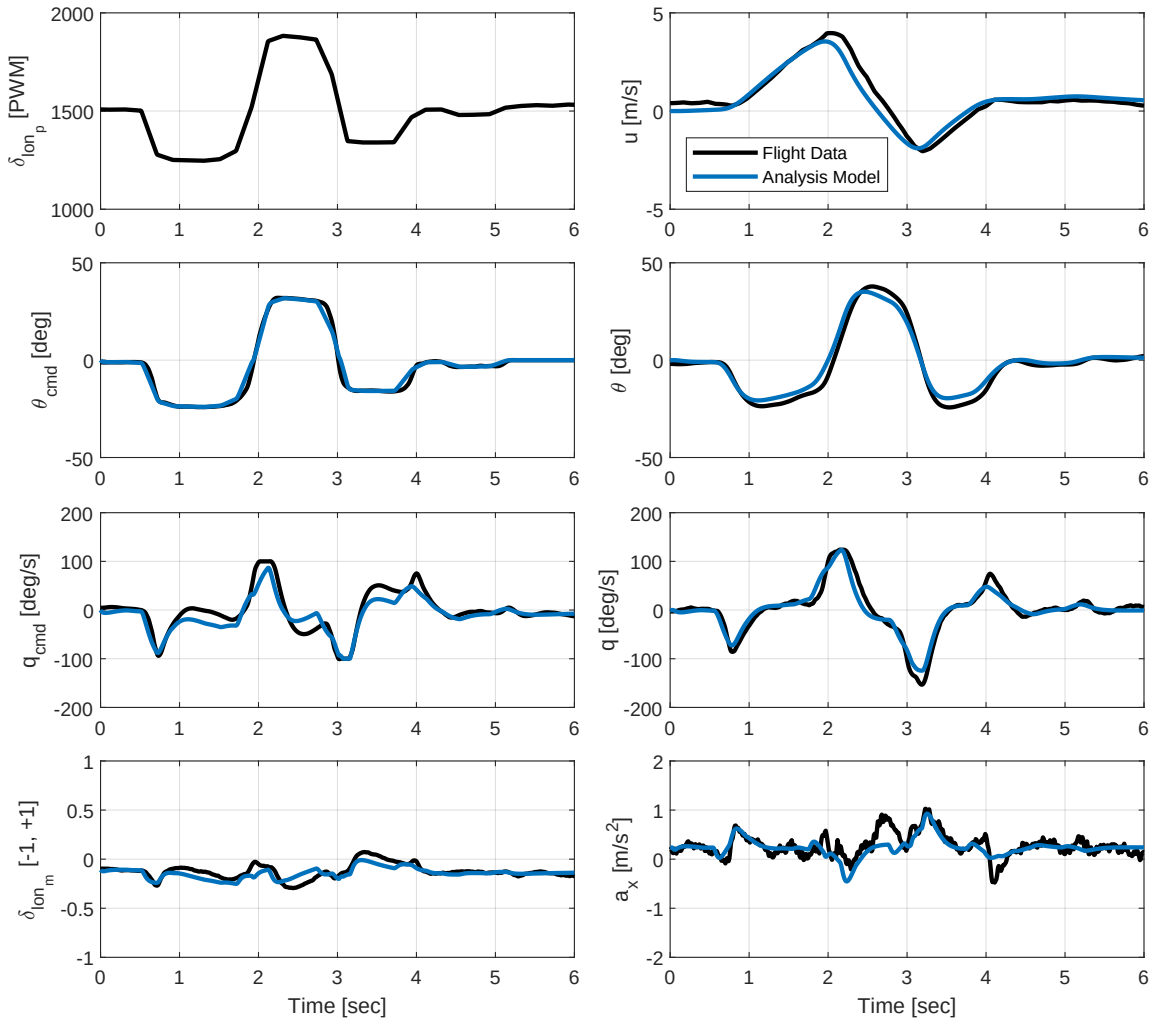

Figure 11: Validation of the analysis model in closed-loop simulation against flight test data for a pitch doublet maneuver.

The baseline gains for pitch and roll axes met all specifications aside from FrqDpG2. There is a general increase in all design parameters for the pitch and roll axes with the most notable increases being the integral gains, mainly driven by the FrqDpG2 specification to improve attitude tracking performance. The baseline yaw axis gains also nearly met all specifications with the exception of the 10% increased stability margins specifications. The baseline yaw rate derivative gain (K_{r_d}) was zero, so that design parameter was fixed at zero given the stable, first-order, yaw axis bare-airframe dynamics. The baseline heave axis met all specifications except RmsAcG1, so there is a general reduction of the heave axis feedback gains to reduce control effort.

Figure 12 shows the on-axis, closed-loop aircraft pitch attitude response to longitudinal input as attained from the analysis model. The magnitude response is seen to decrease at frequencies below 1 rad/s as compared to the optimized design which tracks a constant, steady-state gain value. This results in a baseline aircraft response that initially tracks the pilot input in the short-term with some undershoot, but settles out with significant steady-state error as seen in Fig. 13 which shows a piloted step response time history. The optimized design has a small overshoot but tracks the command with significantly less steady-state error. This small steady-state error cannot be eliminated with the current PX4 attitude control system architecture that uses a proportional gain without any integral action.

Figure 14 shows the magnitude of the pitch attitude disturbance response. The optimized design is seen to have a higher DRB which is evaluated at the -3 dB frequency. The optimized design also has significantly improved attitude disturbance attenuation below 1 rad/s. Figure 15 shows the pitch attitude response of the baseline and optimized designs to a simulated aft gust with a 1-cosine shape and peak magnitude of 1 m/s. While the baseline gains result in a peak pitch attitude excursion of -2.5 degrees, the optimized design reduces it to $\pm$0.5 degrees. The gust input subsides by 1.3 seconds, and the optimized design returns the aircraft to trim by 1.8 seconds whereas the baseline design takes over 6.0 seconds, over 3 times as long, to do so.

Table 7: Baseline versus optimized results for all four axes.

	Roll		Pitch		Yaw		Heave	
	Baseline	Optimized	Baseline	Optimized	Baseline	Optimized	Baseline	Optimized
GM [dB]	12.90	6.65	12.32	6.60	6.44	11.85	14.25	8.95
PM [deg]	70.71	50.01	67.00	50.07	47.31	67.45	71.77	102.42
ω_c [rad/s]	13.20	18.53	13.22	19.48	56.29	29.98	8.87	9.06
DRB [rad/s]	4.65	6.67	4.62	6.25	4.39	4.04	6.93	4.02
DRP [dB]	2.24	4.05	2.43	3.65	0.76	0.97	2.38	1.66

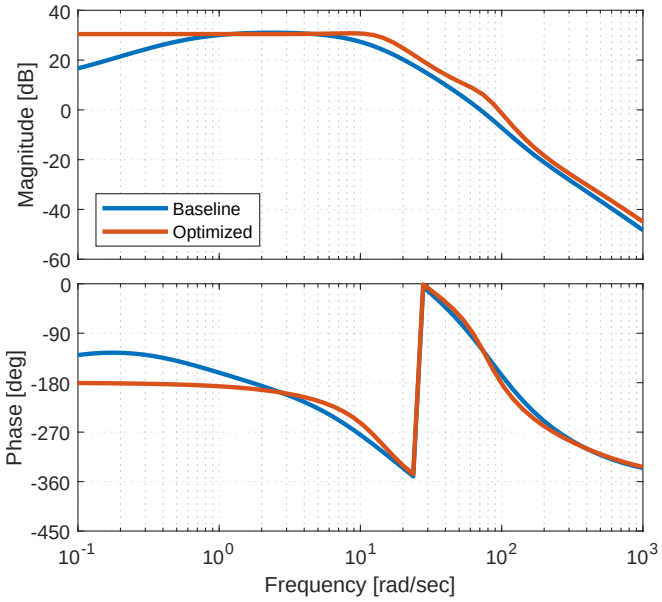

Figure 12: Pitch attitude to longitudinal input frequency response ($\theta/\delta_{\text{lon}}$) from analysis model.

Discussion

The baseline gains were tuned using a trial-and-error approach and resulted in a stable aircraft for flight tests. Further improvement using this method was found to be time-consuming, difficult to evaluate through qualitative means, and potentially dangerous due to the unstable nature of the bare-airframe dynamics. The model-based optimization approach is shown to produce significantly improved command tracking and disturbance rejection performance over the baseline gains while maintaining ample stability margins in simulation.

Though the optimized design provides improvement over the baseline, there are limitations to the attitude command tracking performance due to the inherent architecture of the PX4 inner-loop flight control system. Tracking a step command in attitude with zero steady-state error cannot be achieved with only proportional control on the attitude loops. An integrator and integral gain in the attitude loops are necessary to eliminate the steady-state error and further improve attitude tracking performance. Figure 16 shows the longitudinal axis broken-loop response for the baseline, optimized, and potential third design that utilizes proportional-integral control in the attitude loops. The third design meets all requirements set in Table 5 while providing increased robustness at low frequencies.

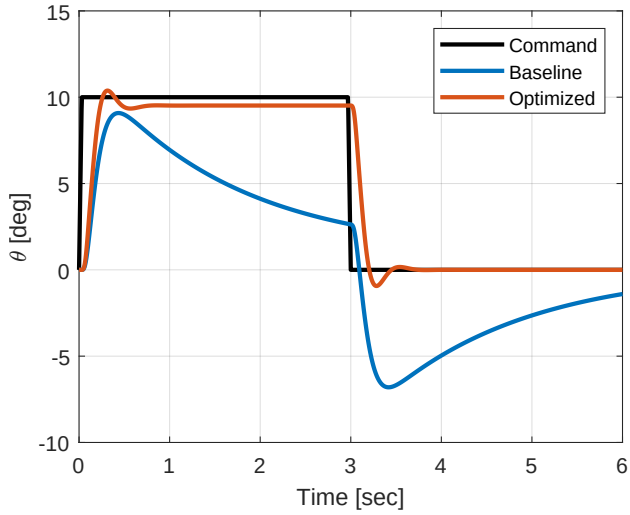

Figure 13: Simulated pitch attitude response due to a 10-degree command for 3 seconds.

CONCLUSIONS

Flight tests were conducted to collect frequency sweeps and doublet data for frequency domain system identification of the UGCR. A hover model of the vehicle was identified and verified using the CIFER® software package. The PX4 inner-loop flight control system was reproduced in simulation, combined with the identified model to form an analysis model and validated against flight test data. The analysis model was used to perform model-based multi-objective optimization of the inner-loop flight control system to improve attitude tracking and disturbance rejection performance over the baseline gain set. The research provided the following conclusions:

1. The UGCR exhibited high frequency vibrations that necessitated higher sample rates to avoid aliasing signals due to undersampling. Higher sampling frequencies can be readily achieved with a combination of hardware and software changes.

2. A 6-DOF hover model of the UGCR is sufficient to capture the bare-airframe flight dynamics within the frequency range of interest for flight control design and

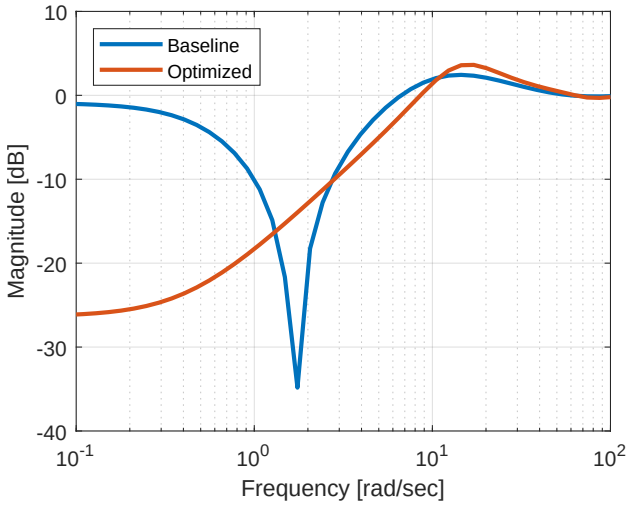

Figure 14: Pitch attitude disturbance rejection response ($\theta/\theta_{\text{dist}}$) from analysis model.

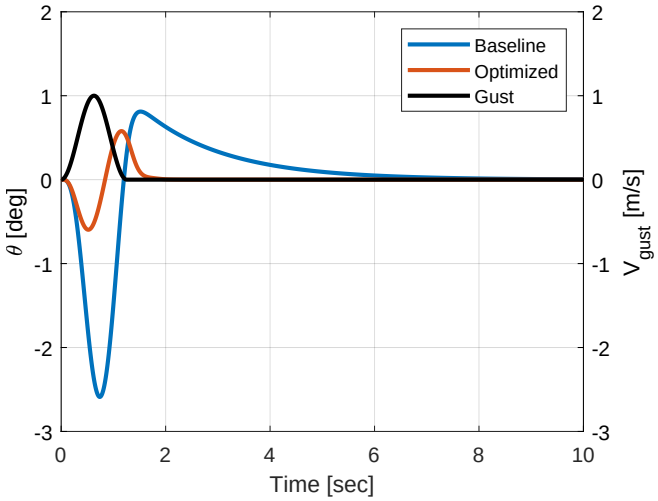

Figure 15: Simulated pitch attitude response to 1-cosine aft gust with 1 m/s peak magnitude.

optimization. The symmetric vehicle configuration is reflected in the expected similarity between identified model parameters in the lateral and longitudinal axes.

3. The model-based optimization approach provides a streamlined method towards tuning of flight control system parameters to improve performance while maintaining closed-loop stability.

4. The addition of an integral gain in the PX4 attitude feedback architecture can improve attitude tracking, disturbance rejection, and eliminate steady-state error.

FUTURE WORK

The improved performance of the optimized flight control system will be validated through flight tests. Forward-flight models of the aircraft will be identified and stitched together with trim data to create a full flight envelope simulation model of the UGCR.

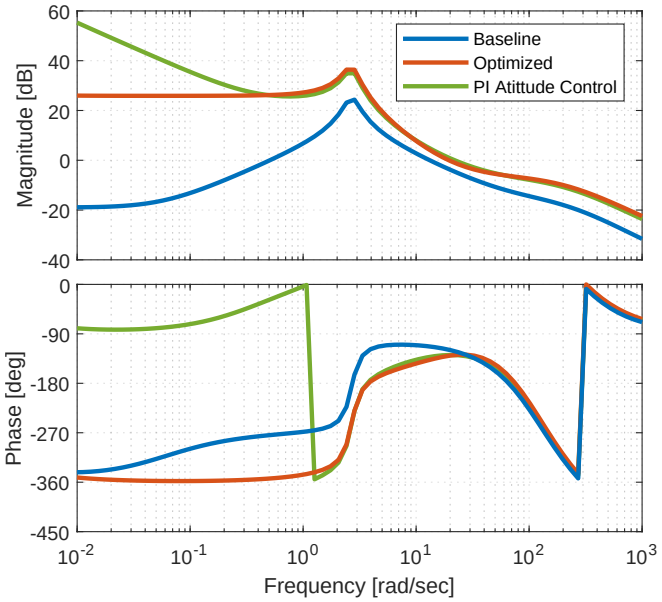

Figure 16: Longitudinal (pitch) axis broken-loop response.

ACKNOWLEDGMENTS

The authors would like to thank the Rafael flight test team and Mr. Assaf Rubannenko for their efforts in operating the aircraft for data collection flights. Additionally, the authors would like to thank the U.S.-Israel Rotorcraft Project Agreement management for their support on this task.

REFERENCES

1. Dadkhah, N., and Mettler, B., "System Identification Modeling and Flight Characteristics Analysis of Miniature Coaxial Helicopter," *Journal of the American Helicopter Society*, Vol. 59, (4), 2014, pp. 36–51. DOI: doi:10.4050/JAHS.59.042011

2. Fujizawa, B. T., Tischler, M., Arlton, P., and Arlton, D., "Control System Development and Flight Testing of the Tiger Moth UAV," American Helicopter Society 68th Annual Forum, May 2012.

3. Bouman, A., Nadan, P., Anderson, M., Pastor, D., Izraelevitz, J., Burdick, J., and Kennedy, B., "Design and autonomous stabilization of a ballistically-launched multirotor," 2020 IEEE International Conference on Robotics and Automation (ICRA), 2020.

4. Tischler, M. B., and Remple, R. K., *Aircraft and Rotorcraft System Identification: Engineering Methods and Flight Test Examples Second Edition*, AIAA education series, American Institute of Aeronautics and Astronautics, Aug 2012. DOI: 10.2514/4.861352

5. Cheung, K. K., Wagster, J. A., Tischler, M. B., Ivler, C. M., Berrios, M. G., Berger, T., Juhasz, O., Tobias, E. L., Goerzen, C. L., Barone, P. S., Sanders, F. C., and Lopez, M. J. S., "An Overview of the U.S. Army Aviation Development Directorate Quadrotor Guidance,

Navigation, and Control Project," American Helicopter Society 73rd Annual Forum, May 2017.

6. Juhasz, O., Tischler, M., and Won, H., "System Identification and Control Law Optimization Applied to the AeroVironment Quantix Tail-Sitter UAS," American Helicopter Society 74th Annual Forum, May 2018.

7. Berrios, M., Berger, T., Tischler, M. B., Juhasz, O., and Sanders, F. C., "Hover Flight Control Design for UAS Using Performance-based Disturbance Rejection Requirements," American Helicopter Society 73rd Annual Forum, May 2017.

8. Tobias, E. L., and Tischler, M. B., "A Model Stitching Architecture for Continuous Full Flight-Envelope Simulation of Fixed-Wing Aircraft and Rotorcraft from Discrete-Point Linear Models," U.S. Army AMRDEC Special Report RDMR-AF-16-01, April 2016.

9. Tobias, E. L., Sanders, F. C., and Tischler, M. B., "Full-Envelope Stitched Simulation Model of a Quadrotor using STITCH," American Helicopter Society 74th Annual Forum, May 2018.

10. Tischler, M. B., Berger, T., Ivler, C. M., Mansur, M. H., Cheung, K. K., and Soong, J. Y., *Practical Methods for Aircraft and Rotorcraft Flight Control Design: An Optimization-based Approach*, AIAA education series, American Institute of Aeronautics and Astronautics, 2017.

11. Berger, T., Ivler, C. M., Berrios, M. G., Tischler, M. B., and Miller, D. G., "Disturbance Rejection Handling Qualities Criteria for Rotorcraft," American Helicopter Society International 72nd Annual Forum Proceedings, May 2016.